Reconstruction of the Magnon Eigenfunctions by X-Ray Magnetic Vector Chronoscopy

Haonan Jin,[1,*] Yuqiang Wang,[2,*] Xinyi He,[1,*] Jingyi Chen,[1] Ethan L. Arnold,[3,4] Gerrit van der Laan,[4] Thorsten Hesjedal,[3,4] Guoqiang Yu[†],[2] and Shilei Zhang[1,†]

[1] *Center for Transformative Science, State Key Laboratory of Quantum Functional Materials, ShanghaiTech Laboratory for Topological Physics, School of Physical Science and Technology, ShanghaiTech University, Shanghai 201210, China*

[2] *Beijing National Laboratory for Condensed Matter Physics, Institute of Physics, Chinese Academy of Sciences, Beijing 100190, China*

[3] *Department of Physics, Clarendon Laboratory, University of Oxford, Oxford OX1 3PU, United Kingdom*

[4] *Diamond Light Source, Harwell Science and Innovation Campus, Didcot OX11 0DE, United Kingdom*

[*] These authors contributed equally to this work.

[†] Corresponding author: guoqiangyu@iphy.ac.cn, shilei.zhang@shanghaitech.edu.cn

The collective precession of magnetization manifests itself as magnon modes. These modes are governed by complex-valued vectorial eigenfunctions, which have remained experimentally challenging to observe. Here we introduce X-Ray Magnetic Vector Chronoscopy (XMVC), a time-resolved resonant scattering method that reconstructs the full magnetization dynamics with angular resolution of $0.1°(\pm 0.01°)$. Applied to a synthetic antiferromagnetic (SAF) multilayer [Si/NiFe (8 nm)/Ru(0.8 nm)/CoFeB (5.5 nm)], XMVC enables magnon state tomography, by directly measuring the nanoscale vectorial eigenfunctions of hybridized modes arising from magnon-magnon coupling. This approach provides full access to the system's non-Hermitian Hamiltonian, revealing the complex-values coupling strengths and non-orthogonal eigenbases. These results establish XMVC as an experimental platform for studying nanoscale spin systems by extracting the eigenfunctions of the system.

In both classical and quantum regimes, the dynamics of a physical system are often governed by an eigenproblem, $\hat{H}|n\rangle = \hbar\omega_n|n\rangle$, where the energy eigenvalues $\hbar\omega_n$ correspond to experimentally observable quantities. Traditional approaches have focused on these eigenvalues, yet the eigenfunctions $|n\rangle$, which define the system's intrinsic state, lie at the core of topological physics [1, 2], non-Hermitian systems [3, 4], quantum information science [5, 6], and so on. These eigenfunctions are typically complex-valued and multi-dimensional, making their full reconstruction experimentally challenging.

This challenge is particularly pronounced in spin-based systems, where the dynamical eigenproblem is mapped onto a set of linearized torque equations [7, 8]. The eigenvalues correspond to resonance frequencies ω_n, while the eigenfunctions $|n\rangle$ represent the time-evolving, complex vectorial modes of magnetization precession. Determining these eigenmodes has profound implications for spintronics, magnonics and quantum information processing [4, 6, 9–15].

In synthetic antiferromagnetic (SAF) multilayers [16, 17], for instance, two degenerate magnon eigenstates can hybridize through breaking rotational symmetry [18–24], forming an effective two-level dissipative dynamical system [3, 4, 25–27], providing an ideal platform for exploring non-Hermitian physics that goes beyond classical magnetism problems. This behaviour shares the same mathematical structure as a two-level spinor system [5, 6, 28–30]. However, the complex Hilbert space of such dissipative magnon systems [4, 25, 31–35] cannot be fully captured through eigenvalues alone. A complete description requires direct, time-resolved measurement of the underlying vectorial eigenfunctions.

State-of-the-art magnetic chronoscopy techniques, such as time-resolved vectorial Kerr imaging [36], x-ray-detected ferromagnetic resonance [37, 38] and magnetic vector nanotomography [39, 40], have proven powerful for probing magnon eigenmodes in magnetic systems. In particular, advanced magnetic imaging chronoscopy methods [39–41] provide vectorial access to the three-dimensional (3D) real-space dynamics, with angular accuracy of the reconstructed order parameter reaching $\sim 0.5^\circ$ [40]. Moreover, the transmission-based geometry [41–45] is ideally suited for studying thinned lamella sample systems. Inspired by these developments, a complementary reflection-based, reciprocal-space-detected chronoscopy technique becomes necessary, especially for ordered magnetic phases in the form of bulk crystals, substrate-supported thin films and heterostructures.

Here, we present a vector chronoscopy technique based on time-resolved resonant elastic

x-ray scattering (REXS), capable of resolving hybridized magnon modes in a SAF system. By combining picosecond temporal resolution [46] with polarization selectivity [47, 48], REXS in reflection geometry becomes directly sensitive to the full vectorial magnetic moment at a fixed scattering condition [48, 49]. In this configuration, all three components of the instantaneous magnetization vector can be simultaneously extracted from a polarization-dependent REXS profile. As a result, XMVC enables high-fidelity access to the transient spin vector with angular accuracy better than 0.1°, alongside efficient data acquisition.

Principles of XMVC. Figure 1a illustrates the XMVC experimental principle, which employs a synchrotron-based stroboscopic technique [37]. A continuous microwave pump and a 35-ps x-ray probe pulse are synchronized with a controlled time delay, operating at a repetition rate of 0.5 GHz. The microwave excitation can be controlled as a single-harmonic signal with frequency ω_{p}, defined as an integer multiple of 0.5 GHz. By tuning the external magnetic field $\mathbf{H}_{\mathrm{dc}}$, the microwave selectively excites a particular magnon resonance mode. At a fixed delay t, the incident x-ray pulses probe a specific phase ($2\pi t/\mathcal{T}$) of the driven magnetization within each modulation period $\mathcal{T}$. The definition of time zero ($t = 0$) is fixed throughout the experiment and detailed in the Supplementary Section 1 and 2.

Using the SAF multilayer as an example, the magnetization in each magnetic layer can be modelled as a macrospin vector $\mathbf{m} = (m_x, m_y, m_z) = (\Theta, \Psi)$, normalized to the saturation magnetization M_S, as shown in Fig. 1b. An arbitrary spin-precessional eigenmode can then be described using a unit sphere representation, in which the magnon state traces a closed-loop, phase-dependent trajectory on the surface of the sphere (Fig. 1c,d). To resolve such modes, we employ a resonant reflectivity geometry [50] [Fig. 1a], where the incidence angle α is half the scattering angle 2α, such that the momentum transfer Q_z corresponds to the specular condition. At a fixed time t and constant Q_z, the transient REXS signal is recorded while continuously scanning the linear polarization angle η from 0° to 180°, probing the instantaneous magnetization vector $\mathbf{m}(t)$. The charge-scattering background is suppressed using a modulation-based filtering technique (Supplementary Section 3). The resulting XMVC dataset takes the form of a two-dimensional polarization-time map, capturing the full vectorial spin dynamics with high angular resolution.

Figure 1e shows a typical XMVC map, numerically generated from the eigenmode in Fig. 1c. Each magnon eigenfunction produces a unique XMVC map, which serves as its

characteristic fingerprint. Consequently, distinct eigenmodes yield fundamentally different XMVC maps, as illustrated in Fig. 1d and 1f. The two-dimensional map exhibits exceptional sensitivity to subtle variations in the spin dynamics, such as the equilibrium macrospin orientation, precession amplitude, ellipticity, and phase. Therefore, once an XMVC map is experimentally obtained, the full vectorial eigenfunction $\mathbf{m}(t)$, parameterized by these quantities, can be reconstructed via an iterative algorithm (Supplementary Section 4 and 5).

Magnon State Tomography. As shown in Fig. 2a, our compensated SAF system consists of two ferromagnetic layers, FM-I (5.5 nm CoFeB, red) and FM-II (8 nm NiFe, green), separated by a 0.8 nm Ru spacer. The antiferromagnetic coupling across the Ru layer gives rise to two orthogonal magnon eigenmodes: the acoustic $|\mathcal{A}\rangle$ and optical $|\mathcal{O}\rangle$ modes [19], whose eigenfunctions are well defined [8]:

$$|\mathcal{A}\rangle = \begin{pmatrix} \mathbf{m}^{\mathrm{I}}_{\mathcal{A}}(t) \\ \mathbf{m}^{\mathrm{II}}_{\mathcal{A}}(t) \end{pmatrix}, \quad |\mathcal{O}\rangle = \begin{pmatrix} \mathbf{m}^{\mathrm{I}}_{\mathcal{O}}(t) \\ \mathbf{m}^{\mathrm{II}}_{\mathcal{O}}(t) \end{pmatrix}. \tag{1}$$

Here, the superscripts (I, II) indicate the FM-I and FM-II layers, while the subscripts $(\mathcal{A}, \mathcal{O})$ denote the acoustic and optical magnon modes, respectively. The explicit forms of the time-dependent magnetization vectors $\mathbf{m}^{\mathrm{I,II}}_{\mathcal{A},\mathcal{O}}(t)$ are provided in Supplementary Section 7.

Breaking the rotational symmetry of the system causes the two magnon modes to couple energetically, forming a two-level spinor system [25, 27, 51]. The resulting Hamiltonian takes the form:

$$\hat{H} = \begin{pmatrix} \hat{a}^\dagger & \hat{b}^\dagger \end{pmatrix} \begin{pmatrix} \hbar\omega_{\mathcal{A}} & \hbar g \\ \hbar g & \hbar\omega_{\mathcal{O}} \end{pmatrix} \begin{pmatrix} \hat{a} \\ \hat{b} \end{pmatrix}, \tag{2}$$

where $\omega_{\mathcal{A}}$ and $\omega_{\mathcal{O}}$ are the eigenfrequencies of the uncoupled acoustic and optical modes. The bosonic operators $\hat{a}$ and $\hat{b}$ obey $[\hat{a}, \hat{a}^\dagger] = 1$ and $[\hat{b}, \hat{b}^\dagger] = 1$, corresponding to the $|\mathcal{A}\rangle$ and $|\mathcal{O}\rangle$ basis states, respectively. Crucially, due to asymmetric damping between FM-I and FM-II [25], the system's coupling strength is complex-valued, $g = g' + ig''$, where the real part g' describes the coherent coupling strength, while the imaginary part g'' quantifies the dissipative coupling. This structure provides a natural platform for exploring non-Hermitian physics [4, 6].

At certain values of the applied field $\mathbf{H}_{\mathrm{dc}}$, a finite coupling g gives rise to new eigenfrequencies and a pair of non-orthogonal hybridized eigenstates, denoted $|-\rangle$ and $|+\rangle$. Diagonalizing the Hamiltonian in Eq. (2) yields eigenvalues ω_- and ω_+ (in units of $\hbar$), along with

a non-unitary basis transformation matrix:

$$U = \begin{pmatrix} u_{\mathcal{A}} & v_{\mathcal{A}} \\ u_{\mathcal{O}} & v_{\mathcal{O}} \end{pmatrix}, \tag{3}$$

which encodes the full mode hybridization. The eigenstates are expressed as:

$$|-\rangle = u_{\mathcal{A}}|\mathcal{A}\rangle + u_{\mathcal{O}}|\mathcal{O}\rangle, \tag{4}$$

$$|+\rangle = v_{\mathcal{A}}|\mathcal{A}\rangle + v_{\mathcal{O}}|\mathcal{O}\rangle. \tag{5}$$

In terms of their layer-resolved magnetization dynamics, the $|-\rangle$ and $|+\rangle$ states are given by:

$$|-\rangle = \begin{pmatrix} \mathbf{m}_{-}^{\mathrm{I}}(t) \\ \mathbf{m}_{-}^{\mathrm{II}}(t) \end{pmatrix}, \quad |+\rangle = \begin{pmatrix} \mathbf{m}_{+}^{\mathrm{I}}(t) \\ \mathbf{m}_{+}^{\mathrm{II}}(t) \end{pmatrix}. \tag{6}$$

Conventional spectroscopic methods, such as ferromagnetic resonance illustrated in Fig. 2b, typically measure only the eigenfrequencies $\omega_{\pm}$, while the corresponding eigenfunctions $|\pm\rangle$ remain inaccessible [25, 27, 29, 30, 34]. By exploiting the element selectivity of soft x-rays, XMVC enables direct, layer-resolved measurement of the vectorial eigenfunctions $\mathbf{m}_{\pm}^{\mathrm{I,II}}(t)$. In other words, the full complex-valued eigenfunctions of $|\pm\rangle$ are experimentally determined, allowing explicit reconstruction of the transformation matrix U.

The experimental determination of the U-matrix has profound implications for magnonics, as it enables *magnon state tomography*, namely the reconstruction concept for a two-level spinor system from experimentally measured observables [5, 52–54]. Here, the tomography approach is formulated within the classical wave framework and enables complete reconstruction of a coherent magnon system's eigenstructure without ambiguity, as illustrated in Fig. 2c. This, in turn, allows for the full knowledge of the non-Hermitian Hamiltonian in Eq. (2) via

$$\begin{pmatrix} \hbar\omega_{\mathcal{A}} & \hbar g \\ \hbar g & \hbar\omega_{\mathcal{O}} \end{pmatrix} = U \begin{pmatrix} \hbar\omega_{-} & 0 \\ 0 & \hbar\omega_{+} \end{pmatrix} U^{-1}, \tag{7}$$

from which the complex-valued coupling strength $g = g' + ig''$ can be quantitatively extracted.

In our experimental configuration, rotational symmetry is broken by applying an rf field $\mathbf{H}_{\mathrm{rf}}$ along the x-axis, while the static field $\mathbf{H}_{\mathrm{dc}}$ is oriented at a 45° elevation within the xz-plane [23, 27], as shown in Fig. 2a. The corresponding field-dependent resonance map, measured *in situ*, is presented in Fig. 2b, where the two hybridized modes $|-\rangle$ and $|+\rangle$

are clearly identified. At $\mu_0 H_{\rm dc} = 58\,\mathrm{mT}$, an anti-crossing feature emerges, signifying an energy gap opening, an effect that has recently attracted significant interest in magnon spectroscopy [14, 21–23, 27, 34, 51, 55–57]. The eigenstates at this field are denoted as $|-'\rangle$ and $|+'\rangle$, reflecting their strongly mixed character.

Magnon Mode Reconstruction. Using the $|+\rangle$ state as an example, we demonstrate how XMVC enables the reconstruction of an arbitrary magnon eigenfunction. The system is driven into resonance by selecting $\omega_{\rm p} = 6\,\mathrm{GHz}$ and $\mu_0 H_{\rm dc} = 44\,\mathrm{mT}$. The probing area, determined by the illuminating beam size, covers 480 μm $\times$ 50 μm on the sample. By tuning the photon energy to the Co or Ni L_3 edge, the time-resolved REXS signal selectively probes the magnetic dynamics in the FM-I and FM-II layers, respectively. Figures 2d and 2e display the XMVC maps for FM-I and FM-II, each exhibiting distinct two-dimensional structure. Through iterative reconstruction, the time evolution of all three magnetization components in each layer is simultaneously retrieved. The resulting precession profiles, i.e, FM-I in red and FM-II in green, are shown in Fig. 2f. This procedure yields the full vectorial eigenfunction of the $|+\rangle$ state, which is visualized on the unit sphere in Fig. 2g (see also Supplementary Movie 1). The reconstructed eigenmode exhibits a fidelity of approximately 0.95, corresponding to an angular resolution of 0.1° with an uncertainty of ±0.01°. As shown in Figs. 2d,e, there is excellent agreement between the measured XMVC maps and those calculated from the reconstructed eigenfunction.

We next examine the full magnon-magnon coupling dynamics at the gap-opening field of $\mu_0 H_{\rm dc} = 58\,\mathrm{mT}$. Following the same XMVC protocol, the time-dependent eigenfunctions of the $|-'\rangle$ and $|+'\rangle$ states are reconstructed and summarized in Fig. 3a,b. To quantitatively compare the relative precession amplitude and phase between FM-I and FM-II, the functions $\mathbf{m}_{\pm}^{\rm I,II}(t)$ are expressed in spherical coordinates $[\Theta_{\pm}^{\rm I,II}(t), \Psi_{\pm}^{\rm I,II}(t)]$, as shown in panels 1. These trajectories can also be visualized on the unit sphere (panels 2), where each mode forms a closed orbit with the $t = 0$ reference phase marked. Supplementary Movies 3,4 show the corresponding real-time dynamics. Although the dc field is applied at a 45° elevation within the xz-plane, both macrospins predominantly precess in the xy-plane due to the easy-plane anisotropy. This results in elliptical precession trajectories that are compressed along the z-axis. For additional insight, panels 3 show top-view projections of the trajectories from each macrospin's time-averaged position. The $t = 0$ positions are marked by larger dots,

and the colour bars trace the temporal evolution. The functions $\mathbf{m}_{\pm}^{\mathrm{I,II}}(t)$ can be parameterized analytically using a set of angular variables: (1) the time-averaged magnetization direction $\mathbf{m}_0 = (\Theta_0, \Psi_0)$, which corresponds to the static magnetization when the microwave excitation is switched off. (2) the precession cone angle ξ along the long axis, and $\beta\xi$ along the short axis, where β is the ellipticity; and (3) the dynamic phase ϕ. Accordingly, the eigenstate of a given mode $|n\rangle$ is fully described by the set:

$$|n\rangle = \begin{pmatrix} \Theta_{0n}^{\mathrm{I}}, \Psi_{0n}^{\mathrm{I}}, \xi_n^{\mathrm{I}}, \beta_n^{\mathrm{I}}, \phi_n^{\mathrm{I}} \\ \Theta_{0n}^{\mathrm{II}}, \Psi_{0n}^{\mathrm{II}}, \xi_n^{\mathrm{II}}, \beta_n^{\mathrm{II}}, \phi_n^{\mathrm{II}} \end{pmatrix}, \tag{8}$$

all of which can be extracted directly from XMVC measurements, as shown in Fig. 3a4,b4.

First, for both $|-'\rangle$ and $|+'\rangle$ states, the time-averaged magnetization directions of the two macrospins are nearly identical but span an asymmetric angle, with the $\mathbf{H}_{\mathrm{dc}}$ vector positioned in between, as shown in Fig. 3a2,b2. This specific static configuration arises from competing interlayer interaction energetics [23, 27, 51], which break the system's two-fold rotational symmetry. As a result, the fundamental acoustic and optical modes $|\mathcal{A}\rangle$ and $|\mathcal{O}\rangle$ become mutually coupled, giving rise to new hybridized eigenstates $|-'\rangle$ and $|+'\rangle$, formed by coherent superpositions of the two bare modes.

Second, the two layers exhibit different damping constants, resulting in exchange loss that competes with the coherent magnon-magnon coupling. This introduces an imaginary component g'' in the coupling strength. The non-Hermitian nature of the system gives rise to several experimentally observable features [4, 6, 25, 27]: (1) The precession amplitudes differ between layers, $\xi^{\mathrm{I}} \neq \xi^{\mathrm{II}}$, and the ratio $\xi^{\mathrm{I}}/\xi^{\mathrm{II}}$ reflects the coherent coupling strength g'. (2) A nontrivial phase difference $\delta\phi = \phi^{\mathrm{I}} - \phi^{\mathrm{II}}$ arises from complex mode hybridization. As shown in Fig. 3a1,b1, this phase offset is neither 0° (in-phase) nor 180° (out-of-phase). Instead, we find $\delta\phi = 50.9°$ for $|-'\rangle$ and 85.5° for $|+'\rangle$, from which g'' can be quantitatively extracted. (3) Most significantly, the hybridized eigenfunctions $|-'\rangle$ and $|+'\rangle$ are non-orthogonal in Hilbert space, a hallmark of non-Hermitian systems, as will be shown below.

Reconstructed Eigenbasis and the non-Hermitian Hamiltonian. With the complete eigenstates experimentally determined (Fig. 3a4,b4), the elements of the U-matrix can be directly extracted, enabling reconstruction of the full non-Hermitian Hamiltonian. Figure 3c presents the results of magnon state tomography, from which the exact eigenvectors are

recovered, revealing how the hybridized $|-'\rangle$ and $|+'\rangle$ states are composed from the uncoupled mode basis. An intuitive way to visualize the $|\pm'\rangle$ states is to map them onto a Bloch sphere [33, 35]. As shown in Fig. 4d, taking $|\mathcal{A}\rangle$ and $|\mathcal{O}\rangle$ as the quantization axis, the hybridized states appear as two distinct vectors. However, they are not located at antipodal points, indicating that the $|-'\rangle$ and $|+'\rangle$ states are non-orthogonal in Hilbert space, a direct consequence of the system's non-Hermitian character. Finally, the full Hamiltonian $\hat{H}$ is reconstructed experimentally (Fig. 3c). The two complex-valued eigenfrequencies are measured to be $\omega_{\mathcal{A}} = (5.307 - 0.567i)\,\mathrm{GHz}$ and $\omega_{\mathcal{O}} = (5.4 - 0.493i)\,\mathrm{GHz}$, where the imaginary components reflect the system's basic loss without the coupling. Crucially, both the coherent coupling strength $g' = 0.398\,\mathrm{GHz}$ and the dissipative component $g'' = -0.27\,\mathrm{GHz}$ are quantitatively extracted, capturing the complete dynamics of the non-Hermitian magnon-magnon coupling process. Moreover, as discussed in Supplementary Section 13, extrinsic inhomogeneous spin-precession dynamics introduces $\sim 0.7\%$ uncertainty in the extracted values of g' and g'' of our SAF system, leaving the non-Hermitian coupling parameters quantitatively robust.

Remarkably, our high-precision XMVC technique reveals that magnon-magnon coupling remains observable even at dc fields away from the gap-opening condition. Figure 4 shows the magnon state tomography results at $\mu_0 H_{\mathrm{dc}} = 44\,\mathrm{mT}$, where the $|-\rangle$ and $|+\rangle$ modes are resolved using the same protocol as in Fig. 3. As shown in panels 1, the macrospins in FM-I and FM-II precess nearly in-phase for the $|-\rangle$ state, and out-of-phase for the $|+\rangle$ state. Without XMVC, these signatures closely resemble those of the uncoupled $|\mathcal{A}\rangle$ and $|\mathcal{O}\rangle$ modes, making them difficult to distinguish. However, full reconstruction of the underlying wavefunctions reveals clear signatures of hybridization. A finite phase shift $\delta\phi_- = 18.8^\circ$ is measured for $|-\rangle$, deviating from the 0° phase expected for $|\mathcal{A}\rangle$. Similarly, $\delta\phi_+ = 190.5^\circ$ is observed for $|+\rangle$, deviating from the 180° value associated with $|\mathcal{O}\rangle$. It is worth noting that the small but non-negligible deviations from 0° or 180° indicate the notable value of g''. Combined with the precession amplitudes $\xi^{\mathrm{I}}/\xi^{\mathrm{II}}$, these deviations provide direct evidence for finite magnon-magnon coupling even in this weakly hybridized regime.

The recovered U-matrix and the corresponding dissipative Hamiltonian are shown in Fig. 4c. At $\mu_0 H_{\mathrm{dc}} = 44\,\mathrm{mT}$, a weaker coherent coupling strength of $g' = 0.287\,\mathrm{GHz}$ is extracted, accompanied by a larger dissipative component $g'' = -0.325\,\mathrm{GHz}$. As shown in Fig. 4d, the eigenstates $|\pm\rangle$ appear nearly orthogonal on the Bloch sphere, closely resembling

the bare modes $|\mathcal{A}\rangle$ and $|\mathcal{O}\rangle$. However, due to the system's non-Hermitian character, the $|\pm\rangle$ states do not lie at antipodal points, confirming their non-orthogonality. Altogether, the full eigenproblem $\hat{H}|\pm\rangle = \hbar\omega_{\pm}|\pm\rangle$ is quantitatively resolved for this hybridized regime, providing unambiguous access to the underlying magnon-magnon coupling dynamics.

Conclusion. Using a SAF multilayer as a model system, we have demonstrated how XMVC enables experimental access to the full eigenproblem in magnetism. Conventional eigenvalue-based approaches typically rely on theoretical or numerical models, which inevitably introduce uncertain parameters and may diverge from the actual physical system. In stark contrast, XMVC provides direct access to the vectorial eigenfunctions, allowing the complete spin dynamics and coupling Hamiltonian to be reconstructed from a single experiment.

On the other hand, two technical limitations of XMVC at its current stage should be noted. First, for disordered spin textures, a scanning-type XMVC approach is required to obtain spatially and temporally resolved mode information. Second, synchrotron-based XMVC is applicable only to magnon systems whose eigenfrequencies lie below approximately 10 GHz, while this constraint can be naturally overcome by implementing the same approach at free-electron laser facilities. Further details are provided in the Supplementary Section 10.

Looking forward, many key topics in spintronics and magnonics — such as spin pumping, spin-torque-based dynamics, magnon-photon coupling, and nonlinear magnonics — ultimately depend on knowledge of the full dynamic mode $\mathbf{m}(t)$. XMVC thus provides an effective route to address these problems by directly measuring the vectorial eigenfunctions $\mathbf{m}(t)$. Moreover, XMVC offers the highest angular resolution to date for characterizing vectorial magnetization dynamics, while its reflection-based geometry is compatible with a wide range of pristine magnetic materials and device architectures, including bulk crystals and substrate-supported thin films.

Acknowledgements

This work was supported by the National Key R&D Program of China (grant no. 2022YFA1403602), the National Natural Science Foundation of China (grant No. 12241406), and the Double First-Class Initiative Fund of ShanghaiTech University. G.Q.Y. acknowledges the CAS Project for Young Scientists in Basic Research (No. YSBR-084) and the CAS Youth Interdisciplinary Team. H.N.J. and Y.Q.W. acknowledge the China Postdoctoral Science Foundation (grant Nos. 2025M773358 and 2025M773402). E.L.A. acknowledges Diamond-EPSRC studentship (2887640, EP/W524311/1). T.H. acknowledges the Oxford-ShanghaiTech collaboration project. Shanghai Synchrotron Radiation Facility and Diamond Light Source are acknowledged for beamtimes.

Author contributions

S.L.Z. conceived the project. S.L.Z. and G.Q.Y. supervised the project. H.N.J., X.Y.H., E.L.A, G.L., T.H., G.Q.Y. and S.L.Z. performed the experiments and analysed the data. Y.Q.W. and G.Q.Y. prepared the samples. Y.Q.W., X.Y.H. and J.Y.C. performed theoretical calculations. S.L.Z. wrote the paper with input from all authors. All authors discussed the results and contents of the paper.

Competing Interests

The authors declare no competing interests.

Figure Captions

FIG. 1. **X-ray magnetic vector chronoscopy (XMVC) measurement principle.** (a) Transient REXS is performed in reflection geometry, using x-ray pulses with a bunch width of 35 ps, synchronized to a master clock operating at 0.5 GHz. The same clock also triggers a synchronized, frequency-multiplied microwave pump with single-harmonic frequency $\omega_{\mathrm{p}} = 0.5$ GHz $\times N$, where N is a selectable integer value. With a controlled delay between pump and probe, the microwave drives the sample into a selected magnon resonance mode. At each fixed point in time, a fixed momentum transfer Q_z is set via the scattering angle 2α, while the incident linear polarization angle η is continuously scanned from 0° to 180°. The resulting XMVC dataset is a two-dimensional polarization-time map, as shown in panels (e) and (f). (b) The transient magnetization vector $\mathbf{m} = (m_x, m_y, m_z)$ is described in spherical coordinates (Θ, Ψ). (c,d) An arbitrary magnon eigenmode $\mathbf{m}(t)$ traces out a closed-loop precession trajectory (red) on the surface of a sphere. Each unique trajectory yields a distinct XMVC map, shown in (e) and (f).

FIG. 2. **XMVC reconstruction of magnon eigenfunctions in a synthetic antiferromagnet.** (a) Magnon-magnon coupling in a balanced SAF structure composed of Si/NiFe (8 nm)/Ru (0.8 nm)/CoFeB (5.5 nm), with the dc magnetic field $\mathbf{H}_{\mathrm{dc}}$ applied at 45° elevation within the xz-plane. The rf-field $\mathbf{H}_{\mathrm{rf}}$ is applied along the x-direction via a coplanar waveguide. The Cartesian coordinate system (x, y, z) is defined to be consistent with the magnetization components (m_x, m_y, m_z). (b) Resonance frequency as a function of $\mathbf{H}_{\mathrm{dc}}$, measured *in situ* using a vector network analyser. Green solid lines indicate theoretically calculated resonance branches. (c) Concept of magnon state tomography, wherein the complex-valued eigenvectors are reconstructed rather than inferred from eigenvalues. (d,e) Experimentally obtained (normalized) XMVC maps for the $|+\rangle$ magnon mode in the FM-I and FM-II layers, respectively. The measurement was performed at 6 GHz under $\mu_0\mathbf{H}_{\mathrm{dc}} = 44\,\mathrm{mT}$. (f) Reconstructed time-dependent magnetization vectors $\mathbf{m}_+^{\mathrm{I}}(t)$ (red) and $\mathbf{m}_+^{\mathrm{II}}(t)$ (green), comprising the full eigenfunction of the $|+\rangle$ state. The error bars represent the standard deviations obtained from ten independent runs of the iterative reconstruction algorithm. (g) Unit sphere representation of the reconstructed $|+\rangle$ eigenfunction. The precession amplitude is magnified by a factor of eight for visual clarity.

FIG. 3. **Magnon state tomography for the $|-'\rangle$ and $|+'\rangle$ eigenstates.** For each mode, panel 1 shows the time-resolved dynamics of $\mathbf{m}^{\mathrm{I}}(t)$ (red) and $\mathbf{m}^{\mathrm{II}}(t)$ (green), represented in spherical coordinates $\Theta^{\mathrm{I,II}}(t)$ and $\Psi^{\mathrm{I,II}}(t)$. The error bars represent the standard deviations obtained from ten independent runs of the iterative reconstruction algorithm. This visualization highlights the relative phase contrast between the two macrospins. Panel 2 depicts the corresponding eigenmode on a unit sphere, where the elliptical trajectory is magnified by a factor of eight for clarity. The red (green) dot marks the $t = 0$ position of FM-I (FM-II). Panel 3 provides an alternative projection, viewing the orbiting trajectory from the time-averaged position of each macrospin. Coloured dots indicate the experimentally sampled time steps, with the larger dot again marking $t = 0$. The temporal evolution follows the gradient of the colour bar. Panel 4 summarises the extracted parameters used to quantify the eigenfunctions, where Θ_0 and Ψ_0 denote the time-averaged magnetization direction; ξ is the cone angle along the long axis of precession; β characterises the ellipticity; and ϕ represents the dynamical phase. (c) Reconstructed U-matrix elements for the rotated basis of $|-'\rangle$ and $|+'\rangle$, from which the effective coupling Hamiltonian is obtained. (d) Bloch sphere representation of the $|-'\rangle$ and $|+'\rangle$ eigenstates in the rotated basis.

FIG. 4. **Magnon state tomography for the $|-\rangle$ and $|+\rangle$ eigenstates.** The representation follows the format of Fig. 3. The XMVC method is applied at a different magnetic field ($\mu_0\mathbf{H}_{\mathrm{dc}} = 44\,\mathrm{mT}$), away from the anti-crossing point, to reconstruct the eigenfunctions of $|-\rangle$ and $|+\rangle$ states. Panels 1-4 show the time-resolved spin dynamics, precession trajectories, trajectory projections, and extracted parameters for the two macrospins, as previously described. The error bars represent the standard deviations obtained from ten independent runs of the iterative reconstruction algorithm. While the $|-\rangle$ and $|+\rangle$ states appear nearly orthogonal on the unit sphere, XMVC reveals measurable phase shifts and amplitude asymmetries, signatures of finite magnon-magnon coupling even outside the strong mixing regime. The reconstructed U-matrix and full non-Hermitian Hamiltonian are shown in panel (c), confirming a weaker coupling strength and enhanced dissipation compared to the $|\pm'\rangle$ case. (d) Bloch sphere representation of the reconstructed $|-\rangle$ and $|+\rangle$ eigenstates, illustrating their near-orthogonal orientation.

References

[1] D. Xiao, M.-C. Chang, and Q. Niu, Berry phase effects on electronic properties, *Rev. Mod. Phys.* **82**, 1959 (2010).

[2] N. Nagaosa and Y. Tokura, Emergent electromagnetism in solids, *Phys. Scr.* **T146**, 014020 (2012).

[3] R. El-Ganainy, K. G. Makris, M. Khajavikhan, Z. H. Musslimani, S. Rotter, and D. N. Christodoulides, Non-hermitian physics and PT symmetry, *Nat. Phys.* **14**, 11-19 (2018).

[4] T. Yu, J. Zou, B. Zeng, J. Rao, and K. Xia, Non-hermitian topological magnonics, *Phys. Rep.* **1062**, 1-86 (2024).

[5] T. D. Ladd, F. Jelezko, R. Laflamme, Y. Nakamura, C. Monroe, and J. L. O'Brien, Quantum computers, *Nature* **464**, 45-53 (2010).

[6] H. Yuan, Y. Cao, A. Kamra, R. A. Duine, and P. Yan, Quantum magnonics: When magnon spintronics meets quantum information science, *Phys. Rep.* **965**, 1-74 (2022).

[7] C. Kittel, On the theory of ferromagnetic resonance absorption, *Phys. Rev.* **73**, 155 (1948).

[8] F. Keffer and C. Kittel, Theory of antiferrornagnetic resonance, *Phys. Rev.* **85**, 329 (1952).

[9] A. V. Chumak, V. I. Vasyuchka, A. A. Serga, and B. Hillebrands, Magnon spintronics, *Nat. Phys.* **11**, 453-461 (2015).

[10] R. A. Duine, K.-J. Lee, S. S. P. Parkin, and M. D. Stiles, Synthetic antiferromagnetic spintronics, *Nat. Phys.* **14**, 217-219 (2018).

[11] P. Pirro, V. I. Vasyuchka, A. A. Serga, and B. Hillebrands, Advances in coherent magnonics, *Nat. Rev. Mater.* **6**, 1114-1135 (2021).

[12] S.-H. Yang, R. Naaman, Y. Paltiel, and S. S. P. Parkin, Chiral spintronics, *Nat. Rev. Phys.* **3**, 328-343 (2021).

[13] J. Han, R. Cheng, L. Liu, H. Ohno, and S. Fukami, Coherent antiferromagnetic spintronics, *Nat. Mater.* **22**, 684-695 (2023).

[14] Y. Zhang, L. Qiu, J. Chen, S. Wu, H. Wang, I. A. Malik, M. Cai, M. Wu, P. Gao, C. Hua, W. Yu, J. Xiao, Y. Jiang, H. Yu, K. Shen, and J. Zhang, Switchable long-distance propagation of chiral magnonic edge states, *Nat. Mater.* **24**, 69-75 (2025).

[15] C. Liu, F. Ai, S. Reisbick, A. Zong, A. Pofelski, M.-G. Han, F. Camino, C. Jing, V. Lomakin,

and Y. Zhu, Correlated spin-wave generation and domain-wall oscillation in a topologically textured magnetic film, *Nat. Mater.* **24**, 406-413 (2025).

[16] P. Grünberg, Magnetostatic spinwave modes of a ferromagnetic double layer, *J. Appl. Phys.* **51**, 4338-4341 (1980).

[17] P. Grünberg, Magnetostatic spin-wave modes of a heterogeneous ferromagnetic double layer, *J. Appl. Phys.* **52**, 6824-6829 (1981).

[18] P. Grünberg, R. Schreiber, and Y. Pang, Layered magnetic structures: Evidence for antiferromagnetic coupling of Fe layers across Cr interlayers, *Phys. Rev. Lett.* **57**, 2442 (1986).

[19] J. J. Krebs, P. Lubitz, A. Chaiken, and G. A. Prinz, Magnetic resonance deterination of the antiferromagnetic coupling of Fe layers through Cr, *Phys. Rev. Lett.* **63**, 1645 (1989).

[20] B. Heinrich, Y. Tserkovnyak, G. Woltersdorf, A. Brataas, R. Urban, and G. E. W. Bauer, Dynamic exchange coupling in magnetic bilayers, *Phys. Rev. Lett.* **90**, 187601 (2003).

[21] S. Klingler, V. Amin, S. Geprägs, K. Ganzhorn, H. Maier-Flaig, M. Althammer, H. Huebl, R. Gross, R. D. McMichael, M. D. Stiles, S. T. Goennenwein, and M. Weiler, Spin-torque excitation of perpendicular standing spin waves in coupled YIG/Co heterostructures, *Phys. Rev. Lett.* **120**, 127201 (2018).

[22] J. Chen, C. Liu, T. Liu, Y. Xiao, K. Xia, G. E. Bauer, M. Wu, and H. Yu, Strong interlayer magnon-magnon coupling in magnetic metal-insulator hybrid nanostructures, *Phys. Rev. Lett.* **120**, 217202 (2018).

[23] D. MacNeill, J. T. Hou, D. R. Klein, P. Zhang, P. Jarillo-Herrero, and L. Liu, Gigahertz frequency antiferromagnetic resonance and strong magnon-magnon coupling in the layered crystal $CrCl_3$, *Phys. Rev. Lett.* **123**, 047204 (2019).

[24] A. B. et al., The 2021 magnonics roadmap, *J. Phys.: Condens. Matter* **33**, 413001 (2021).

[25] H. Liu, D. Sun, C. Zhang, M. Groesbeck, R. Mclaughlin, and Z. V. Vardeny, Observation of exceptional points in magnonic parity-time symmetry devices, *Sci. Adv.* **5**, eaax9144 (2019).

[26] B. Hu, Z. K. Xie, J. Lu, and W. He, *arXiv* , 2308.14463 (2023).

[27] Y. Wang, Y. Zhang, C. Li, J. Wei, B. He, H. Xu, J. Xia, X. Luo, J. Li, J. Dong, W. He, Z. Yan, W. Yang, F. Ma, G. Chai, P. Yan, C. Wan, X. Han, and G. Yu, Ultrastrong to nearly deep-strong magnon-magnon coupling with a high degree of freedom in synthetic antiferromagnets, *Nat. Commun.* **15**, 2077 (2024).

[28] X. Zhang, C.-L. Zou, L. Jiang, and H. X. Tang, Strongly coupled magnons and cavity mi-

crowave photons, *Phys. Rev. Lett.* **113**, 156401 (2014).

[29] Y. Tabuchi, S. Ishino, A. Noguchi, T. Ishikawa, R. Yamazaki, K. Usami, and Y. Nakamura, Coherent coupling between a ferromagnetic magnon and a superconducting qubit, *Science* **349**, 405-408 (2015).

[30] D. Lachance-Quirion, S. P. Wolski, Y. Tabuchi, S. Kono, K. Usami, and Y. Nakamura, Entanglement-based single-shot detection of a single magnon with a superconducting qubit, *Science* **367**, 425-428 (2020).

[31] M. W. Daniels, R. Cheng, W. Yu, J. Xiao, and D. Xiao, Nonabelian magnonics in antiferromagnets, *Phys. Rev. B* **98**, 134450 (2018).

[32] T. Wimmer, A. Kamra, J. Gückelhorn, M. Opel, S. Geprägs, R. Gross, H. Huebl, and M. Althammer, Observation of antiferromagnetic magnon pseudospin dynamics and the Hanle effect, *Phys. Rev. Lett.* **125**, 247204 (2020).

[33] A. Kamra, T. Wimmer, H. Huebl, and M. Althammer, Antiferromagnetic magnon pseudospin: Dynamics and diffusive transport, *Phys. Rev. B* **102**, 174445 (2020).

[34] M. Ishibashi, Y. Shiota, T. Li, S. Funada, T. Moriyama, and T. Ono, Switchable giant nonreciprocal frequency shift of propagating spin waves in synthetic antiferromagnets, *Sci. Adv.* **6**, eaaz6931 (2020).

[35] B. Hu, Z.-K. Xie, J. Lu, and W. He, Mapping the magnon–magnon hybrid state onto the Bloch sphere, *Appl. Phys. Lett.* **124**, 232402 (2024).

[36] Y. Acremann, C. H. Back, M. Buess, O. Portmann, A. Vaterlaus, D. Pescia, and H. Melchior, Imaging precessional motion of the magnetization vector, *Science* **290**, 492-495 (2000).

[37] D. A. Arena, E. Vescovo, C.-C. Kao, Y. Guan, and W. E. Bailey, Weakly coupled motion of individual layers in ferromagnetic resonance, *Phys. Rev. B* **74**, 064409 (2006).

[38] G. van der Laan, Time-resolved X-ray detected ferromagnetic resonance of spin currents, *J. Electron Spectrosc. Relat. Phenom.* **220**, 137-146 (2017).

[39] C. Donnelly, S. Finizio, S. Gliga, M. Holler, A. Hrabec, M. Odstrčil, S. Mayr, V. Scagnoli, L. J. Heyderman, M. Guizar-Sicairos, and J. Raabe, Time-resolved imaging of three-dimensional nanoscale magnetization dynamics, *Nat. Nanotech.* **15**, 356-360 (2020).

[40] D. Girardi, S. Finizio, C. Donnelly, G. Rubini, S. Mayr, V. Levati, S. Cuccurullo, F. Maspero, J. Raabe, D. Petti, and E. Albisetti, Three-dimensional spin-wave dynamics, localization and interference in a synthetic antiferromagnet, *Nat. Commun.* **15**, 3057 (2024).

[41] S. Wintz, V. Tiberkevich, M. Weigand, J. Raabe, J. Lindner, A. Erbe, A. Slavin, and J. Fassbender, Magnetic vortex cores as tunable spin-wave emitters, *Nat. Nanotech.* **11**, 948-953 (2016).

[42] C. Donnelly, S. Gliga, V. Scagnoli, M. Holler, J. Raabe, L. J. Heyderman, and M. Guizar-Sicairos, Tomographic reconstruction of a three-dimensional magnetization vector field, *New J. Phys.* **20**, 083009 (2018).

[43] C. Donnelly, A. Hierro-Rodríguez, C. Abert, K. Witte, L. Skoric, D. Sanz-Hernández, S. Finizio, F. Meng, S. McVitie, J. Raabe, D. Suess, R. Cowburn, and A. Fernández-Pacheco, Complex free-space magnetic field textures induced by three-dimensional magnetic nanostructures, *Nat. Nanotech.* **17**, 136-142 (2022).

[44] A. Rana, C.-T. Liao, E. Iacocca, J. Zou, M. Pham, X. Lu, E.-E. C. Subramanian, Y. H. Lo, S. A. Ryan, C. S. Bevis, R. M. Karl, A. J. Glaid, J. Rable, P. Mahale, J. Hirst, T. Ostler, W. Liu, C. M. O'Leary, Y.-S. Yu, K. Bustillo, H. Ohldag, D. A. Shapiro, S. Yazdi, T. E. Mallouk, S. J. Osher, H. C. Kapteyn, V. H. Crespi, J. V. Badding, Y. Tserkovnyak, M. M. Murnane, and J. Miao, Three-dimensional topological magnetic monopoles and their interactions in a ferromagnetic meta-lattice, *Nat. Nanotech.* **18**, 227-232 (2023).

[45] J. Neethirajan, B. J. Daurer, M. D. P. Martínez, A. Hrabec, L. Turnbull, R. Yamamoto, M. R. Ferreira, A. Štefančič, D. A. Mayoh, G. Balakrishnan, Z. Pei, P. Xue, L. Chang, E. Ringe, R. Harrison, S. Valencia, M. Kazemian, B. Kaulich, and C. Donnelly, Soft x-ray phase nanomicroscopy of micrometer-thick magnets, *Phys. Rev. X* **14**, 031028 (2024).

[46] D. M. Burn, S. L. Zhang, G. Q. Yu, Y. Guang, H. J. Chen, X. P. Qiu, G. van der Laan, and T. Hesjedal, Depth-resolved magnetization dynamics revealed by x-ray reflectometry ferromagnetic resonance, *Phys. Rev. Lett.* **125**, 137201 (2020).

[47] C. Mazzoli, S. B. Wilkins, S. Di Matteo, B. Detlefs, C. Detlefs, V. Scagnoli, L. Paolasini, and P. Ghigna, Disentangling multipole resonances through a full x-ray polarization analysis, *Phys. Rev. B* **76**, 195118 (2007).

[48] S. L. Zhang, G. van der Laan, and T. Hesjedal, Direct experimental determination of the topological winding number of skyrmions in Cu_2OSeO_3, *Nat. Commun.* **8**, 14619 (2017).

[49] S. Zhang, G. van der Laan, W. Wang, A. Haghighirad, and T. Hesjedal, Direct observation of twisted surface skyrmions in bulk crystals, *Phys. Rev. Lett.* **120**, 227202 (2018).

[50] Y. Guang, K. Ran, J. Zhang, Y. Liu, S. Zhang, X. Qiu, Y. Peng, X. Zhang, M. Weigand,

J. Gräfe, G. Schütz, G. van der Laan, T. Hesjedal, S. Zhang, G. Yu, and X. Han, Superposition of emergent monopole and antimonopole in CoTb thin films, *Phys. Rev. Lett.* **127**, 217201 (2021).

[51] M. Li, J. Lu, and W. He, Symmetry breaking induced magnon-magnon coupling in synthetic antiferromagnets, *Phys. Rev. B* **103**, 064429 (2021).

[52] K. Vogel and H. Risken, Determination of quasiprobability distributions in terms of probability distributions for the rotated quadrature phase, *Phys. Rev. A* **40**, 2847 (1989).

[53] C.-R. Yi, J. Yu, H. Yuan, R.-H. Jiao, Y.-M. Yang, X. Jiang, J.-Y. Zhang, S. Chen, and J.-W. Pan, Extracting the quantum geometric tensor of an optical raman lattice by bloch-state tomography, *Phys. Rev. Res.* **5**, L032016 (2023).

[54] S. Sharma, S. Viola Kusminskiy, and V. A. S. V. Bittencourt, Quantum tomography of magnons using brillouin light scattering, *Phys. Rev. B* **110**, 014416 (2024).

[55] Y. Shiota, T. Taniguchi, M. Ishibashi, T. Moriyama, and T. Ono, Tunable magnon-magnon coupling mediated by dynamic dipolar interaction in synthetic antiferromagnets, *Phys. Rev. Lett.* **125**, 017203 (2020).

[56] A. Sud, C. W. Zollitsch, A. Kamimaki, T. Dion, S. Khan, S. Iihama, S. Mizukami, and H. Kurebayashi, Tunable magnon-magnon coupling in synthetic antiferromagnets, *Phys. Rev. B* **102**, 100403 (2020).

[57] A. H. Comstock, C.-T. Chou, Z. Wang, T. Wang, R. Song, J. Sklenar, A. Amassian, W. Zhang, H. Lu, L. Liu, M. C. Beard, and D. Sun, Hybrid magnonics in hybrid perovskite antiferromagnets, *Nat. Commun.* **14**, 1834 (2023)

Methods

Sample preparation

The synthetic antiferromagnet sample was deposited at room temperature on a thermally oxidized, 100 μm-thick Si substrate using an ultra-high vacuum magnetron sputtering system. The film stack is as follows: $Si/SiO_2/Pt(3\,nm)/Ni_{80}Fe_{20}(8\,nm)/Ru(0.8\,nm)/Co_{20}Fe_{60}B_{20}(5.5\,nm)/Pt(3\,nm)$, where the bottom and top Pt layers act as seed and capping layers, respectively.

REXS setup

XMVC measurements were carried out using a soft x-ray diffractometer, and all measurements were performed in reflection geometry for REXS [46, 49, 50]. The incident angle α can be continuously tuned from 0° to 180° with a resolution of 0.01°. The external magnetic field $\mathbf{H}_{\rm dc}$ is coupled to the α-axis and rotates together with it, maintaining a fixed angle γ_H with respect to the sample surface. In this work, to maximize the gap-opening effect at the $|\pm'\rangle$ state, the field orientation is configured to $\gamma_H = 45°$ within the xz-plane [23, 27, 51].

An independent detector arm set to a scattering angle of 2α is used to detect the REXS signal at selected momentum transfer Q_z, given by $Q_z = 2k\sin\alpha$, where k is the wavevector of the incident x-rays. We use photon energies of 778.4 eV and 852.5 eV to selectively probe the CoFeB (FM-I) and NiFe (FM-II) layers, respectively. The corresponding optimized scattering angles are $2\alpha = 10°$ for FM-I and $2\alpha = 12°$ for FM-II. Once the scattering angle 2α is fixed, the magnetization vector $\mathbf{m}$ is probed via an η-scan, in which the incident linear polarization angle η is continuously varied from 0° to 180°. Here, $\eta = 0°$ corresponds to horizontal polarization, while $\eta = 90°$ corresponds to vertical polarization.

XMVC setup

XMVC is implemented using a tailored synchrotron-based stroboscopic technique. The 500 MHz master clock of the synchrotron is used to synchronize the microwave excitation with the x-ray pulse train. The clock signal is frequency-multiplied by a controllable integer number using a comb generator and bandpass filters to produce a single-harmonic microwave drive with a frequency of ω_p. We use $\omega_{\rm p} = 4$, 5, 5.5, and 6 GHz to selectively excite the $|-\rangle$, $|-'\rangle$, $|+'\rangle$, and $|+\rangle$ modes, respectively. The microwave signal is subsequently modulated, delayed, and amplified before being injected into a coplanar waveguide underneath

the sample.

To isolate the time-dependent magnetic response, the microwave excitation is modulated on and off at a local oscillation frequency of 4.137 kHz. The resulting lock-in signal, recorded by a fast photodiode with the sampling rate of 200 MHz, provides a direct measurement of the XMVC signal. At each fixed delay time t and momentum transfer Q_z, the transient magnetization vector $\mathbf{m}(t)$ is extracted by analysing the polarization-dependent XMVC. The detailed reconstruction method is documented in Supplementary Section 4 and 5.

Data availability

The data that support the findings of this study are made in public and are available at https://doi.org/10.5281/zenodo.18028719.

Code availability

The code that implements the XMVC calculations is available from the corresponding authors upon request.

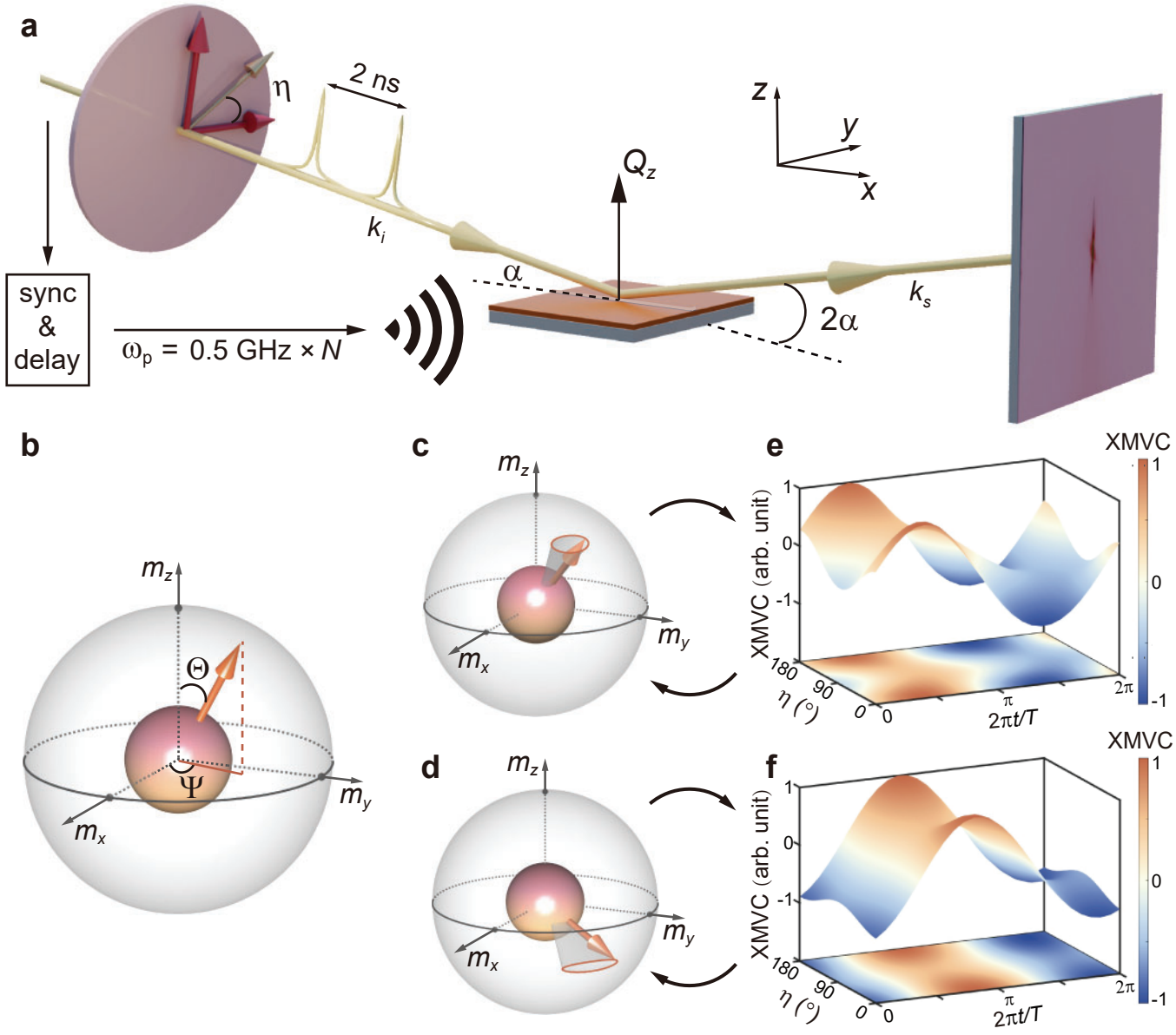
a
η
2 ns
k_i
Q_z
z
y
x
α
2α
k_s
sync & delay
ω_p = 0.5 GHz × N
b
m_z
Θ
Ψ
m_x
m_y
c
m_z
m_y
m_x
d
m_z
m_y
m_x
e
XMVC
XMVC (arb. unit)
η (°)
2πt/T
f
XMVC
XMVC (arb. unit)
η (°)
2πt/T

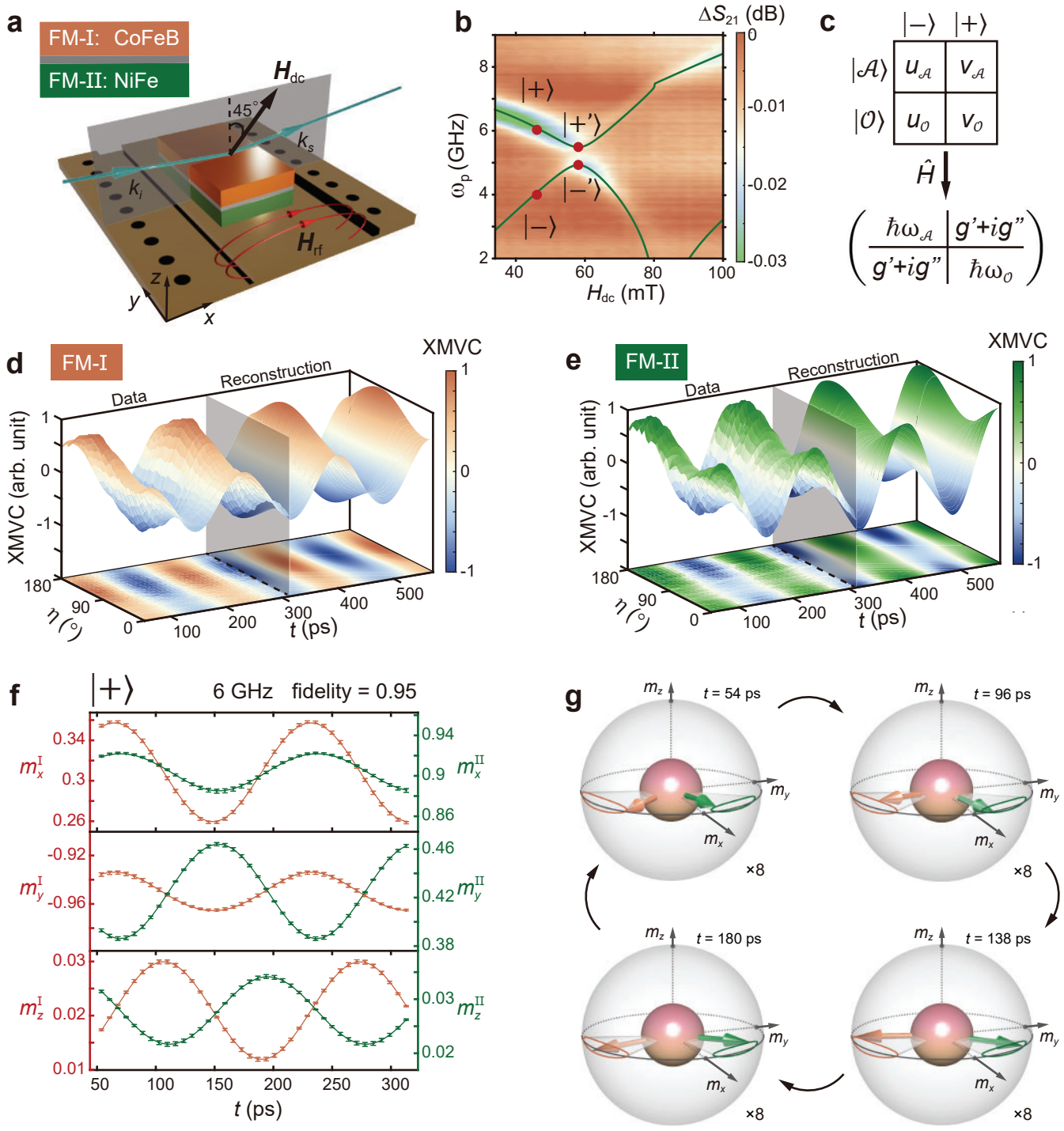
a
FM-I: CoFeB
FM-II: NiFe
H_{dc}
45°
k_s
k_i
H_{rf}
z
y
x
b
ΔS_{21} (dB)
0
-0.01
-0.02
-0.03
$|+\rangle$
$|+'\rangle$
$|-'\rangle$
$|-\rangle$
ω_p (GHz)
H_{dc} (mT)
c
$|-\rangle$ $|+\rangle$
$|\mathcal{A}\rangle$ $u_{\mathcal{A}}$ $v_{\mathcal{A}}$
$|\mathcal{O}\rangle$ $u_{\mathcal{O}}$ $v_{\mathcal{O}}$
$\hat{H}$
$\hbar\omega_{\mathcal{A}}$ $g'+ig''$
$g'-ig''$ $\hbar\omega_{\mathcal{O}}$
d
FM-I
Data
Reconstruction
XMVC
XMVC (arb. unit)
η (°)
t (ps)
e
FM-II
Data
Reconstruction
XMVC
XMVC (arb. unit)
η (°)
t (ps)
f
$|+\rangle$
6 GHz fidelity = 0.95
m_x^I
m_y^I
m_z^I
m_x^{II}
m_y^{II}
m_z^{II}
t (ps)
g
t = 54 ps
t = 96 ps
t = 180 ps
t = 138 ps
m_z
m_y
m_x
×8

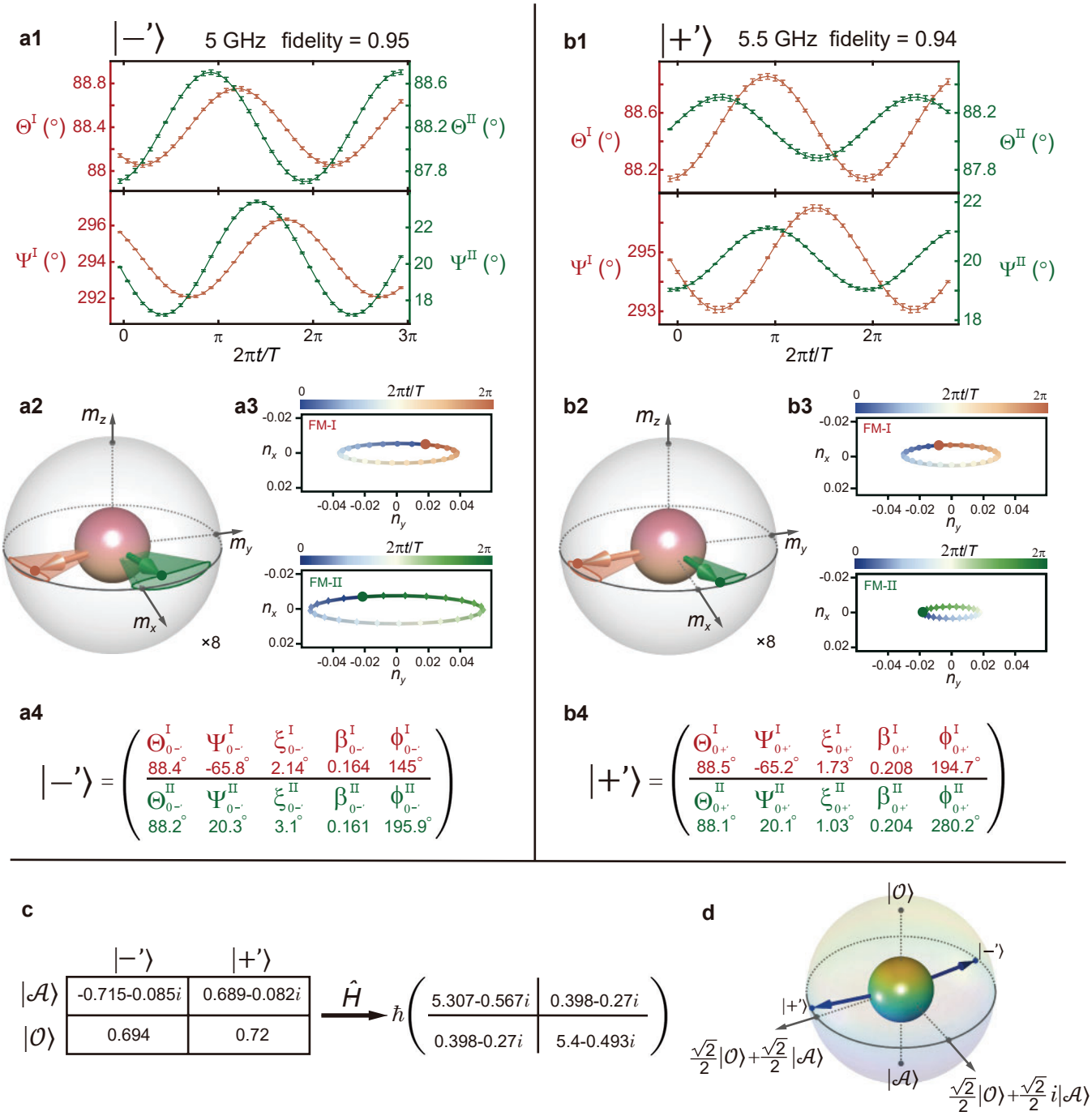
a1
$|-'\rangle$ 5 GHz fidelity = 0.95
Θ^{I} (°)
Θ^{II} (°)
Ψ^{I} (°)
Ψ^{II} (°)
$2\pi t/T$
a2
m_z
m_y
m_x
×8
a3
FM-I
FM-II
n_x
n_y
b1
$|+'\rangle$ 5.5 GHz fidelity = 0.94
b2
b3
a4
$|-'\rangle = \left(\begin{array}{ccccc} \Theta^{I}_{0-'} & \Psi^{I}_{0-'} & \xi^{I}_{0-'} & \beta^{I}_{0-'} & \phi^{I}_{0-'} \\ 88.4^{\circ} & -65.8^{\circ} & 2.14^{\circ} & 0.164 & 145^{\circ} \\ \hline \Theta^{II}_{0-'} & \Psi^{II}_{0-'} & \xi^{II}_{0-'} & \beta^{II}_{0-'} & \phi^{II}_{0-'} \\ 88.2^{\circ} & 20.3^{\circ} & 3.1^{\circ} & 0.161 & 195.9^{\circ} \end{array}\right)$
b4
$|+'\rangle = \left(\begin{array}{ccccc} \Theta^{I}_{0+'} & \Psi^{I}_{0+'} & \xi^{I}_{0+'} & \beta^{I}_{0+'} & \phi^{I}_{0+'} \\ 88.5^{\circ} & -65.2^{\circ} & 1.73^{\circ} & 0.208 & 194.7^{\circ} \\ \hline \Theta^{II}_{0+'} & \Psi^{II}_{0+'} & \xi^{II}_{0+'} & \beta^{II}_{0+'} & \phi^{II}_{0+'} \\ 88.1^{\circ} & 20.1^{\circ} & 1.03^{\circ} & 0.204 & 280.2^{\circ} \end{array}\right)$
c
$|-'\rangle$ $|+'\rangle$
$|\mathcal{A}\rangle$ -0.715-0.085i 0.689-0.082i
$|\mathcal{O}\rangle$ 0.694 0.72
$\hat{H}$
$\hbar\begin{pmatrix} 5.307-0.567i & 0.398-0.27i \\ 0.398-0.27i & 5.4-0.493i \end{pmatrix}$
d
$|\mathcal{O}\rangle$
$|-'\rangle$
$|+'\rangle$
$|\mathcal{A}\rangle$
$\frac{\sqrt{2}}{2}|\mathcal{O}\rangle+\frac{\sqrt{2}}{2}|\mathcal{A}\rangle$
$\frac{\sqrt{2}}{2}|\mathcal{O}\rangle+\frac{\sqrt{2}}{2}i|\mathcal{A}\rangle$

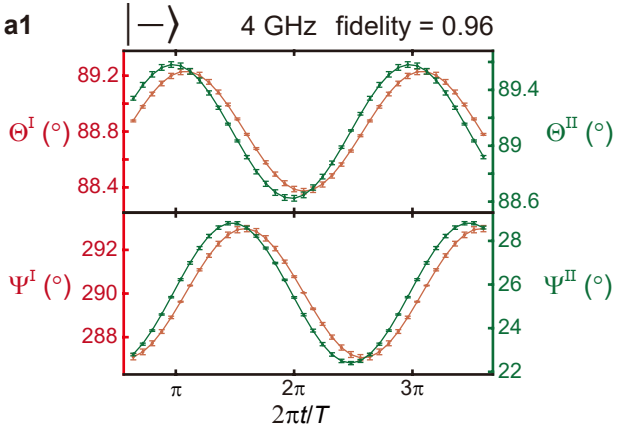

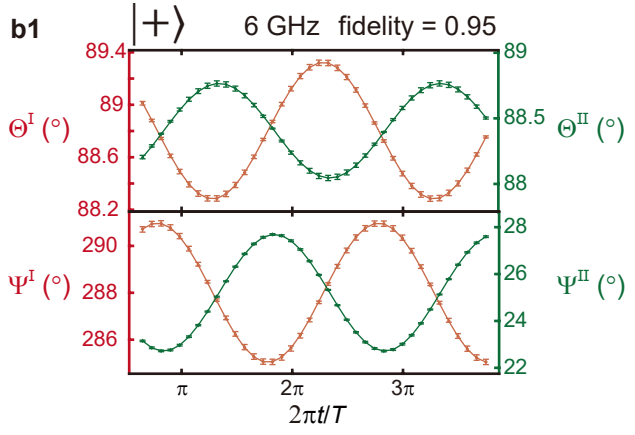

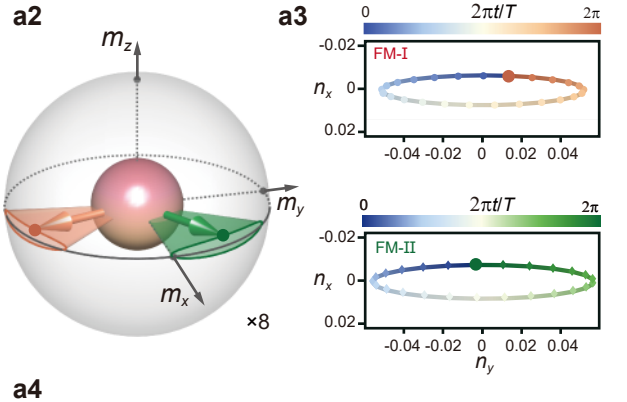

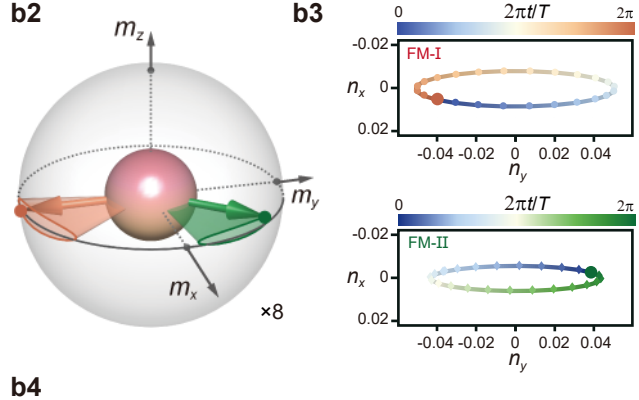

a4

$$|-\rangle = \left(\begin{array}{ccccc} \Theta^{I}_{0-} & \Psi^{I}_{0-} & \xi^{I}_{0-} & \beta^{I}_{0-} & \phi^{I}_{0-} \\ 88.8^{\circ} & -70^{\circ} & 2.97^{\circ} & 0.145 & 165.2^{\circ} \\ \hline \Theta^{II}_{0-} & \Psi^{II}_{0-} & \xi^{II}_{0-} & \beta^{II}_{0-} & \phi^{II}_{0-} \\ 89.1^{\circ} & 25.6^{\circ} & 3.22^{\circ} & 0.149 & 184^{\circ} \end{array}\right)$$

b4

$$|+\rangle = \left(\begin{array}{ccccc} \Theta^{I}_{0+} & \Psi^{I}_{0+} & \xi^{I}_{0+} & \beta^{I}_{0+} & \phi^{I}_{0+} \\ 88.8^{\circ} & -72^{\circ} & 3.02^{\circ} & 0.175 & 309.7^{\circ} \\ \hline \Theta^{II}_{0+} & \Psi^{II}_{0+} & \xi^{II}_{0+} & \beta^{II}_{0+} & \phi^{II}_{0+} \\ 88.4^{\circ} & 25.2^{\circ} & 2.48^{\circ} & 0.145 & 119.2^{\circ} \end{array}\right)$$

c

	$\|-\rangle$	$\|+\rangle$
$\|\mathcal{A}\rangle$	-0.68-0.713i	0.119-0.125i
$\|\mathcal{O}\rangle$	0.172	0.985

$$\xrightarrow{\hat{H}} \hbar \left(\begin{array}{cc} 3.782\text{-}0.306i & 0.287\text{-}0.325i \\ 0.287\text{-}0.325i & 6.264\text{-}0.324i \end{array}\right)$$

d